Journal of Energy Storage 73 (2023) 109202

Contents lists available at ScienceDirect

Journal of Energy Storage

journal homepage: www.elsevier.com/locate/est

Research papers

Unified model of lithium-ion battery and electrochemical storage system

Simone Barcellona *, Silvia Colnago, Lorenzo Codecasa, Luigi Piegari

Department of Electronics, Information and Bioengineering, Politecnico di Milano, Italy

ARTICLE INFO

Keywords:
Lithium-ion battery
Battery electrical model
Electrochemical storage systems
Characterization procedure

ABSTRACT

Nowadays, energy storage systems are of paramount importance in sectors such as renewable energy production and sustainable mobility because of the energy crisis and climate change issues. Although there are various types of energy storage systems, electrochemical devices such as electric double layer capacitors (EDLCs), lithium-ion capacitors (LiCs), and lithium-ion batteries (LiBs) are the most common because of their high efficiency and flexibility. In particular, LiBs are broadly employed in many applications and preferred in the mobility sector, where there is a need for high energy and high power. To ensure good operating conditions for a battery and limit its degradation, it is important to have a precise model of the device. The literature contains numerous equivalent circuit models capable of predicting the electrical behavior of an LiB in the time or frequency domain. In most of them, the battery impedance is in series with a voltage source modeling the open circuit voltage of the battery for simulation in the time domain. This study demonstrated that an extension of a model composed exclusively of passive elements from the literature for EDLCs and LiCs would also be suitable for LiBs, resulting in a unified model for these types of electrochemical storage systems. This model uses the finite space Warburg impedance, which, in addition to the diffusion process of lithium\lithium ions in the electrodes\electrolyte, makes it possible to consider the main capacitance of the battery. Finally, experimental tests were performed to validate the proposed model.

1. Introduction

The energy crisis and climate change are spurring researchers in the energy sector to find new solutions for renewable energy production and sustainable mobility. Energy storage systems are of paramount importance in the development of both technologies. There are several different energy storage devices, which can be classified as mechanical, chemical, biological, thermal, electrical, and electrochemical [1]. Among these, electrochemical devices are the most commonly used because of their high efficiency and flexibility [2]. They are especially preferred in the mobility sector, where there is a need for high-energy and high-power devices. Electrochemical energy storage systems can be divided in two main types: open systems such as fuel cells and flow batteries and closed systems such as batteries and supercapacitors [3]. The latter were the focus of the present work, in which it was proven that a model proposed in the literature for both electric double layer capacitors (EDLCs) and lithium-ion capacitors (LiCs) is also suitable for lithium-ion batteries (LiBs), leading to a unified model for these types of electrochemical storage systems.

It is possible to find numerous studies in the literature related to modeling the electrical, thermal, or aging behavior of LiBs. The approach to develop such a model can be physical, mathematical, or circuital [4]. The first approach models LiBs using very detailed chemical equations, resulting in a very precise model, but requires a large amount of computational time. The second approach describes the external behavior of a battery with simple equations, without exploiting the physical principles based on the cell. This approach leads to a less precise model, but is very easy to implement in a battery management system and requires little computational time. The circuital approach uses lumped circuit elements to represent the different phenomena. This approach is the most commonly used in real applications because it ensures high precision with low complexity [5].

Equivalent circuit models are widely used in the literature to represent the thermal [6–8] or electrical behavior, potentially considering aging aspects [9,10], of LiBs. This paper focuses on the electrical one. The simplest equivalent circuit model consists of a voltage source, which represents the open circuit voltage of the battery (i.e., the voltage when no current flows) and a resistor in series, which represents the battery's internal impedance [11,12]. This model is very simple and has just two parameters to be fit, but it is not capable of modeling the

* Corresponding author.
E-mail address: simone.barcellona@polimi.it (S. Barcellona).

https://doi.org/10.1016/j.est.2023.109202
Received 14 March 2023; Received in revised form 15 September 2023; Accepted 4 October 2023
Available online 10 October 2023

dynamics of the battery and, therefore, cannot be used in applications where a certain accuracy must be ensured. To overcome this issue, the so-called Thevenin model was used in [10,13,14]. In this model, some parallel RC branches in series with the resistor are added. This makes it possible to also model the dynamics of the battery, with more parallel RC branches leading to greater precision for the model [4]. It is worth noting that the former simplest equivalent circuit model can be seen as a particular case of the Thevenin model with zero parallel RC branches. Therefore, we can generalize these models and refer to them as nth-order Thevenin models, where the number of parallel RC branches determines the value of n, and the total number of parameters is $2n + 2$ [15]. Lastly, a very precise and detailed model, in which the different lumped elements correspond to different physical phenomena, was employed in [9,16,17], and consisted of a voltage source in series with four elements: a resistor, two ZARC impedances, and a Warburg impedance, with a total of ten or even more parameters. The series resistor models the internal resistance due to the ohmic resistance of the battery cell; the ZARC elements, which are generalized parallel RC branches based on the usage of constant phase elements (CPEs), model the dynamics related to the solid electrolyte interface (SEI), charge transfer process, and double layer effect. The Warburg impedance makes it possible to model the slow dynamic processes happening inside the battery, i.e., the diffusion processes. According to the target accuracy and aspect to be modeled, either only one ZARC element can be used for modeling the charge transfer process [18], or both ZARC elements can be employed without the Warburg impedance [19]. On the other hand, in many cases, the two ZARC impedances are replaced with two simple parallel RC branches, as a second-order Thevenin model [20–22].

In some cases, the battery parameters are kept constant [12], whereas in other cases they depend on working conditions such as the temperature [23,24], state of charge (SOC) [17,25,26], or aging conditions [9,10]. Moreover, there are many different methods to evaluate them. These methods can be divided in time-domain and frequency-domain methods. Pulse-charge and pulse-discharge experiments were performed in [15,27] to derive the parameters of the Thevenin model. In [28,29], the authors derived the parameters through a complete discharge at constant current, while in [30] a hybrid pulse power characteristic test and Federal Urban Driving Schedule were used for the parameter estimation. For frequency-domain methods, electrochemical impedance spectroscopy (EIS), in which a small amplitude sinusoidal current or voltage at different frequencies is applied to the device, is generally performed to derive the parameters of complex equivalent circuit models [31,32]. In this way, it is possible to derive the impedance value at every tested frequency, and the parameters of the equivalent circuit are, in turn, derived from the resulting spectrum. Many studies can be found in the literature that analyzed different aspects of the equivalent impedance. In [17], several different EIS tests were performed to study the influences of the current rate, temperature, and SOC on the battery impedance, while in [23,33], EIS tests were used to see how temperature affects the different impedances of the battery equivalent circuit model. In [34], EIS was used to study the impact of the relaxation time on the battery impedance. EIS was also used to study the state of health (SOH) of the battery: in [35], EIS was used to analyze the effect of the calendar aging on battery impedance, while in [9,16], the cycle aging effect on impedance was analyzed.

In most of the aforementioned models, the voltage source representing the open circuit voltage, as a function of the SOC, was placed in series with the equivalent impedance. Indeed, the latter was used to model the internal resistance and dynamic behavior of the battery, while the voltage source was used to model the electrical energy stored in the form of chemical energy in the battery. Nevertheless, even if the voltage source as a function of the SOC correctly models such a phenomenon, from a conceptual point of view, the use of a voltage source is better suited to modeling open systems in which, in addition to an electric port, other ports of different types such as mechanical or chemical ones are accessible. In fact, in these cases, the voltage source models a continuous conversion of energy from one form to another through the different ports. For example, in electrical generators, mechanical energy (entering the mechanical port) is turned into electric energy (leaving the electric port) continuously, with the opposite occurring for electric motors. In fuel cells and flow batteries, the accessible chemical port is used to continuously fill the chemical energy, which is converted into electrical energy. On the other hand, in LiBs, which are closed systems, similar to EDLCs and LiCs, there is no continuous conversion of energy between two or more different ports, but the energy is stored and released only using the electric port, i.e., they can only accumulate and decumulate energy. For this reason, conceptually, LiBs should be better modeled as big capacitors. Of course, the main difference between LiBs and EDLCs is the physical kind of energy conversion and storage. In fact, in EDLCs, which are composed of two porous carbon electrodes, during the charging phase, the electric energy is turned into dielectric energy and stored through the electric field in the dielectric medium (inner Helmholtz plane), with the opposite occurring during the discharging phase. In LiBs, which are usually composed of an anode made of lithiated graphite and a cathode made of a lithium metal oxide, during the charging phase, the electric energy is turned into chemical energy and stored through electrochemical reactions (lithium-ion intercalation and de-intercalation), with the opposite occurring during the discharging phase. Finally, LiCs, which are a hybridization between an EDLC and LiB, with an anode made of a lithium metal oxide like an LiB and a cathode made of porous carbon like an EDLC, store and release electric energy in both ways. Therefore, LiBs can be modeled using chemical capacitors. EDLCs can be modeled using electric capacitors, and LiCs can be modeled using both. Nonetheless, in all cases, from the electric terminal point of view, capacitors are seen as equivalent electric capacitors. This assumption is supported in different works [36,37].

Moreover, in the authors' opinion, the correct choice for the Warburg impedance, in addition to the diffusion processes, can also be used to represent a large capacitor in relation to the stored energy, just like for EDLCs and LiCs. Therefore, the voltage source can be removed from the equivalent circuit model. In [37–39], a model without the voltage source was employed for the analysis, but only the frequency behavior and impedance spectrum were considered for validation, and the time domain behavior of the model was not exploited. The electric circuit model proposed in [40,41] was used to model the behavior of both EDLCs and LiCs in the full frequency range, and its extension, proposed in [42], was used to model LiCs even in a wide temperature range.

In the present work, the latter model was further expanded to test its usability in modeling the behavior of LiBs, leading to a unified electric storage system (UESS) model. Moreover, a hybrid procedure that relies on both time- and frequency-domain methods for parameter estimation is presented. Finally, experimental characterization tests and the validation of the proposed model were performed and analyzed.

2. Proposed unified electric storage system (UESS) model

In the literature, one of the most common electric circuit models used to represent the electrical behavior of LiBs, in a wide frequency range, is the one reported in Fig. 1a. It is composed of an ideal voltage source, which represents the open circuit voltage of the battery as a function of the SOC, in series with four impedance terms that can also be functions of the SOC. Of course, all these parameters can depend on other factors such as the temperature, SOH, and current. The current study only considered the dependency on the open circuit voltage. The frequency response (Nyquist plot) of such an electric model is reported in Fig. 1b.

The first term is the ohmic resistor R_s, which represents the electronic resistance of the current collectors, terminals, and electrodes, along with the ionic resistance of the electrolyte, and corresponds to the intersection with the real axis of the Nyquist plot in the high-frequency region. The second term is the parallel RC branch composed of resistor R_{SEI} and capacitor C_{SEI}, which is related to the SEI and corresponds to the first semi-circle in the medium–high-frequency region of the Nyquist plot.

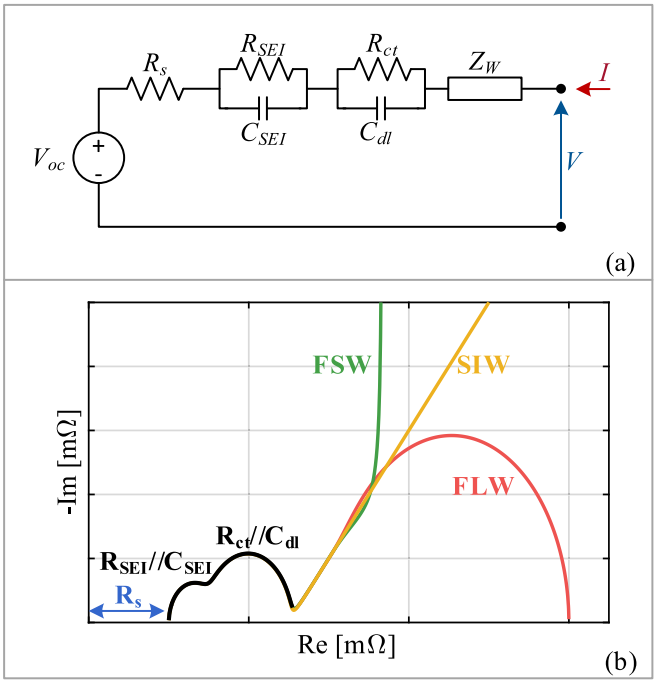

Fig. 1. a) Equivalent electric circuit; b) Nyquist plot of the impedance spectrum.

The third term is the parallel RC branch composed of resistor R_{ct} and capacitor C_{dl}, which represent the charge transfer chemical reaction and electric double layer capacitance effect, respectively, and corresponds to the second semi-circle in the medium–low-frequency region of the Nyquist plot. Finally, the last term is the Warburg impedance Z_W, which is related to the diffusion processes of the lithium inside the electrodes and lithium-ions inside the electrolyte and corresponds to the low-frequency region of the Nyquist plot. In the literature, it is possible to find three main different kinds of Warburg elements that are used to model the lithium/lithium-ion diffusion processes. The first is a semi-infinite length Warburg (SIW) element that models a semi-infinite diffusion layer and shows an oblique line with a slope of 45° in the Nyquist plot. The related mathematical equation, in the frequency domain, is as follows:

$$Z_{SIW} = A_d \frac{1}{\sqrt{j\omega}}, \tag{1}$$

where A_d is the diffusion coefficient.

The second is a finite-space Warburg (FSW) element that models a limited diffusion layer with an impermeable boundary and shows a first part with an oblique line with a slope of 45° followed by a vertical line in the Nyquist plot. The latter part models the capacitive behavior. The related mathematical equation, in the frequency domain, is as follows:

$$Z_{FSW} = R_d \frac{coth(\sqrt{j\omega R_d C_d})}{\sqrt{j\omega R_d C_d}}, \tag{2}$$

where R_d and C_d are the resistance and capacitance, respectively, related to the diffusion processes.

The last is a finite-length Warburg (FLW) element that models a limited diffusion layer with a transmissive boundary and shows a first part with an oblique line with a slope of 45° followed by a big semi-circle in the Nyquist-plot. The related mathematical equation, in the frequency domain, is as follows:

$$Z_{FLW} = R_d \frac{tanh(\sqrt{j\omega R_d C_d})}{\sqrt{j\omega R_d C_d}}. \tag{3}$$

The SIW element is not consistent with the real behavior because the lithium diffusion into the electrodes and lithium-ion diffusion into the electrolyte must be completed when the lithium/lithium-ions reach the boundary of the electrolyte or electrodes themselves. Conversely, the FLW element can be used to model the lithium-ion diffusion into the electrolyte because when the lithium-ions reach the electrode/electrolyte interface the intercalation/de-intercalation processes occur and it behaves as transmissive boundary [43]. Instead, the FSW element can be used to model the lithium diffusion in the active material of the electrodes, which is blocked by the impermeable wall of the current collectors [43]. Of course, because of the diffusion processes of the lithium/lithium-ions in both the electrodes and electrolyte, the two effects are superimposed in the low-frequency region [43]. Therefore, at very low frequencies, the electric model of a LiB should have both FSW and FLW elements or another more general Warburg element that can consider both phenomena. In any case, the lithium diffusion into the electrodes, limited by the impermeable current collectors, makes the entire battery behave like a large capacitor. Therefore, for the sake of simplicity, the FSW element is chosen to model all the diffusion processes in this analysis.

According to this assumption, unlike many works found in the literature, the ideal voltage source can be eliminated from the model, obtaining the impedance model reported in Fig. 2a. In fact, one of the main aspects highlighted here is that the FSW element not only can model the diffusion processes of the lithium/lithium-ions, but can also model a large chemical capacitance related to the intercalation/de-intercalation chemical reactions, which are related to the energy stored in the battery. Therefore, the related mathematical equation in the frequency domain is as follows:

$$Z_p(j\omega, V_{oc}) = R_s(V_{oc}) + \frac{R_{SEI}(V_{oc})}{1 + j\omega R_{SEI}(V_{oc}) C_{SEI}(V_{oc})} + \frac{R_{ct}(V_{oc})}{1 + j\omega R_{ct}(V_{oc}) C_{dl}(V_{oc})} + R_d(V_{oc}) \frac{coth\left(\sqrt{j\omega R_d(V_{oc}) C_d(V_{oc})}\right)}{\sqrt{j\omega R_d(V_{oc}) C_d(V_{oc})}} =$$
$$= R_p(\omega, V_{oc}) + \frac{1}{j\omega C_p(\omega, V_{oc})}, \tag{4}$$

where all the parameters are function of open circuit voltage V_{oc}. In this way, we obtain a more general unified model with seven parameters, which includes as subcases the ones used in [40–42] to model both EDLCs and LiCs. Indeed, in [40], the proposed electric model for EDLCs is composed of only one series resistor, related to the ohmic resistance of the electrodes and electrolyte, and one FSW impedance, which considers the diffusion process and adsorption\desorption of the solvated ions into the porous carbon electrodes of EDLCs. In [41], the same model was applied to LiCs at room temperature, while in [42], the model was expanded by adding one parallel RC branch that considered the charge transfer and electric double layer effect related to the lithium metal oxide electrode of LiCs, which at low temperatures exhibit a behavior like LiBs. The model used in this work, for LiBs, is the same of the one used in [42], but with a further additional parallel RC branch that also models the behavior of SEI.

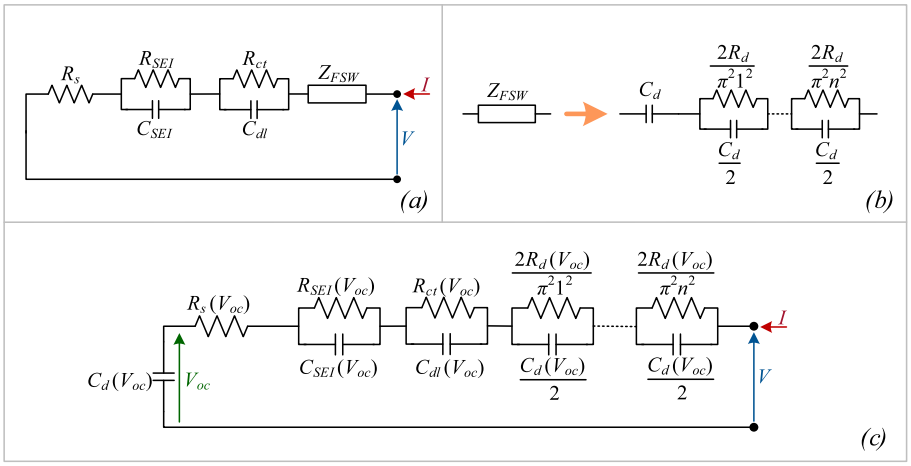

Fig. 2. a) Impedance model; b) expansion of the FSW; c) proposed UESS model.

To obtain an equivalent electric circuit model composed only of RC elements, we need to perform the inverse Laplace transformation of the FSW term. Unfortunately, the latter is very complicated to solve. However, it could be simplified as reported in [44], according to which the FSW term can be expanded as an infinite series of parallel RC branches, as reported in Fig. 2b. From a practical point of view, six branches are sufficient to approximate the Warburg term in a good way. In any case, for any approximation number, there are always seven different parameters. Finally, as reported in [40], it is possible to write the following:

$$\lim_{\omega\to 0}\Re e\{Z_p\} = R_s + R_{SEI} + R_{ct} + \sum_{n=1}^{\infty}\frac{2}{n^2\pi^2}R_d = R_s + R_{SEI} + R_{ct} + \frac{R_d}{3}$$

$$\lim_{\omega\to\infty}\Re e\{Z_p\} = R_s \tag{5}$$

$$\lim_{\omega\to 0}\Im m\{\omega Z_p\} = -\frac{1}{C_d}.$$

From Eq. (5), it is possible to recognize the physical meaning of the terms. The dc resistance of the battery is given by the sum of all the resistance contributions: the ohmic resistance, SEI resistance, charge transfer resistance, and diffusion resistance terms. It is worth noting that the latter term is divided by a factor 3. The high-frequency resistance is equal to the ohmic resistance, R_s. Finally, the dc capacitance is equal to the diffusion capacitance, and it is related to the intercalation/de-intercalation processes into the electrodes. The complete proposed UESS model is reported in Fig. 2c.

3. Test procedure and experimental setup

In this work, a lithium cobalt oxide (LCO) battery pouch cell (8773160K) manufactured by General Electronics Battery Co. Ltd. was used to validate the proposed model. This type of battery is composed of a cathode made of lithium cobalt oxide, an anode made of graphite, and these two electrodes are separated by a polymer electrolyte. The battery specifications are reported in Table 1. Fig. 3 shows the experimental setup. The latter was composed of a potentiostat (SP-150) connected to 100 A booster (VMP3B-100), both manufactured by Biologic Science Instrument, and both connected via ethernet to a PC, which controlled them through the EC-Lab software.

Table 1
Battery specifications.

Parameter	Value
Nominal capacity	10 Ah
Maximum voltage	4.2 V
Discharge cut-off voltage	2.75 V
Maximum continuous discharge current	100 A (10C)

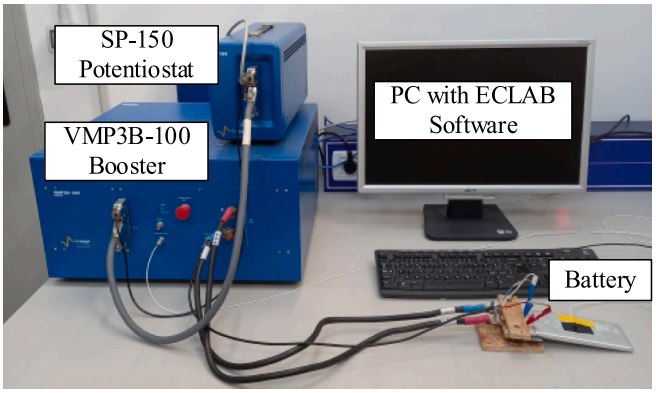

Fig. 3. Experimental setup.

In [40–42], the parameters of the electric circuit model were found using the simple galvanostatic electrochemical impedance spectroscopy (GEIS) technique. The latter consists in supplying the storage device under test with a sinusoidal current, superimposed to a given polarization voltage, and obtaining the resulting voltage waveform. Through the ratio between the current and voltage waveform, in the frequency domain, a complex impedance value is obtained at a given frequency. By sweeping the frequencies over a certain interval, a complex impedance frequency response can be obtained. In [40–42], the frequency range used to extract the parameters of the model, applied to EDLC and LiC devices, was between 10 mHz and 100 Hz or 100 mHz and 100 Hz. On the other hand, for LiB devices, the frequency range needed to exploit the frequency response able to discern all the impedance terms of the proposed model was much larger. To analysis the capacitive behavior of the battery, we would need to perform GEIS measurements at very low frequencies up to 0.1 mHz [30]. This would be a very hard task because the GEIS measurements at those low frequencies would be too long and could become unstable, giving incorrect results.

In light of the above, the proposed test procedure was based on a combination of both frequency-domain and time-domain methods, and all the tests were performed at room temperature (20 °C). In particular, two kinds of test were performed: the open circuit voltage (V_{oc}) discharge curve measurement in the time domain and GEIS measurements in the frequency domain. The former gave information about the low-frequency behavior of the battery, while the latter were used to extract the parameters related to the medium–high-frequency region.

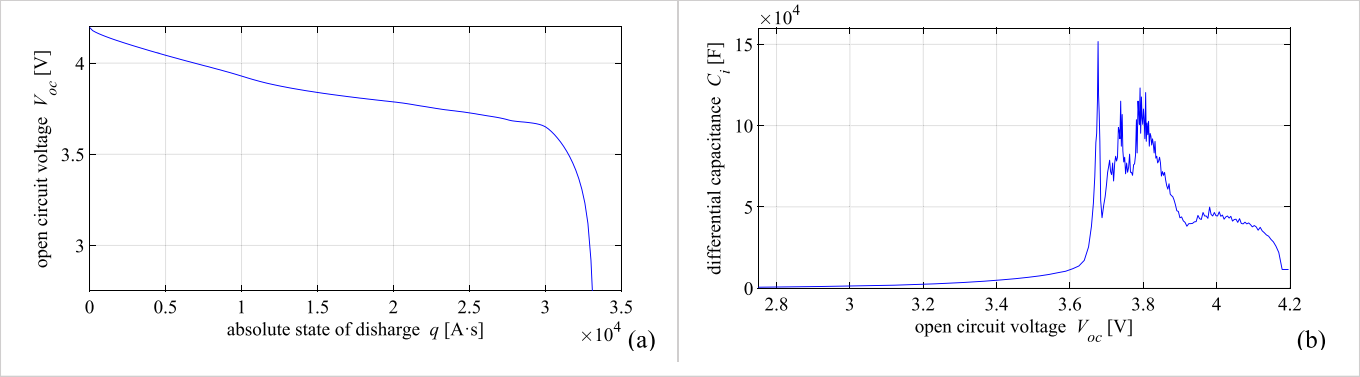

Fig. 4. a) Open circuit voltage curve; b) differential capacitance of LiB under test.

3.1. Open circuit voltage measurement

The open circuit voltage curve measurement was performed by discharging the battery at a very low current rate to neglect the voltage drop over the internal resistance and related dynamics. To do this, the battery was fully charged using the constant current–constant voltage (CC-CV) protocol. In the first step, a constant current of 10 A (1C) was applied to reach the maximum cut-off voltage of 4.2 V. In the second step, the same voltage of 4.2 V was applied until the current was lower than 200 mA (0.02C). Afterward, a discharge at a constant current of 200 mA (0.02C) was performed until the battery voltage reached the cut-off value of 2.75 V, and the open circuit voltage curve was obtained. This curve was expressed as a function of the absolute state of discharge q in A·s, obtaining the $V_{oc}(q)$ function. From the latter, using the inverse function $q(V_{oc})$, it was possible to obtain the so-called differential or incremental capacitance, as follows:

$$C_i(V_{oc}) = \frac{dq(V_{oc})}{dV_{oc}}. \tag{6}$$

3.2. Galvanostatic electrochemical impedance spectroscopy measurements

The GEIS measurements were performed in a frequency range of 100 mHz–10 kHz for a set of different open circuit voltages, V_{oc}, between 2.8 V and 4.2 V, with voltage steps of 0.1 V. Thus, a total of 15 GEIS measurements were performed. The battery was first fully charged using the CC-CV protocol with a constant current of 10 A (1C) to reach the maximum cut-off voltage of 4.2 V. Then, the same voltage of 4.2 V was applied until the current was lower than 200 mA (0.02C). It is worth noting that, when the latter step was completed, an electric transient occurred that was related to the different electrochemical mechanisms, which were modeled with the parallel RC branches and FSW element with different time constants. Considering the largest one, which was related to the lithium/lithium-ion diffusion, the battery was left to rest for 1 h, and then the GEIS measurement was performed. Afterward, the battery was discharged with a constant current of 10 A (1C) to reach 4.1 V, and the latter was applied until the current was lower than 200 mA (0.02C). At this new open circuit voltage, after 1 h of resting, another GEIS measurement was performed. The same procedure was repeated, discharging the battery by 0.1 V at a time until 2.8 V was reached. In this way, it was possible to obtain the frequency response of the battery in the medium–high-frequency region for the different open circuit voltages.

The crucial point of this procedure was to combine the information retrieved by the two kinds of tests. In fact, it is possible to demonstrate, in a straightforward way, as reported in [45], that differential capacitance $C_i(V_{oc})$ equates with the equivalent capacitance $C_p(\omega,V_{oc})$, obtained from the GEIS measurements, when the frequency tends to zero. This means that, according to the proposed model and Eq. (5), diffusion capacitance $C_d(V_{oc})$ is equal to the differential capacitance $C_i(V_{oc})$. Therefore, it was possible to fit the GEIS experimental data using Eq. (4) by fixing the value of diffusion capacitance C_d according to the value of differential capacitance C_i. Furthermore, the value of ohmic resistance R_s was fixed by taking the experimental value of the frequency response that corresponds to the intersection with the real axis of the Nyquist plot. Therefore, for each open circuit voltage V_{oc}, the other five parameters (R_{SEI}, C_{SEI}, R_{ct}, C_{dl}, and R_d) were evaluated using the complex least-square minimization method applied to Eq. (4). To minimize the error of a complex quantity, the total vector error was used and applied to the following function:

$$\varepsilon = \sqrt{\left(\frac{\left\|R_p - R_p^*\right\|}{\left\|R_p^*\right\|}\right)^2 + \left(\frac{\left\|C_p - C_p^*\right\|}{\left\|C_p^*\right\|}\right)^2} \tag{7}$$

where $\boldsymbol{R}_p^*$ and $\boldsymbol{C}_p^*$ are the vectors of the experimental measurements of the real and imaginary parts, respectively, of impedance $\boldsymbol{Z}_p$, while $\boldsymbol{R}_p$ and $\boldsymbol{C}_p$ are the vectors of the related values obtained using Eq. (4). The five parameters were found using this minimization procedure.

Finally, all the parameters could be stored in look-up tables or fitted as functions of voltage V_{oc}.

4. Characterization test results

According to the procedure reported in the previous section, Fig. 4a shows open circuit voltage $V_{oc}(q)$ obtained through the discharge curve measurement performed in the time domain. After that, according to Eq. (6), the differential capacitance $C_i(V_{oc})$, reported in Fig. 4b, was calculated. From Fig. 4b, it is possible to identify the characteristic peaks of the differential capacity for an LCO battery during the discharging phase. These peaks correspond to specific structural phase transitions occurring within the electrodes during the intercalation and deintercalation processes, as reported in [46]. In particular, the cathode undergoes structural changes between hexagonal-I, hexagonal-II, and monoclinic structures of the lithium cobalt oxide. On the other hand, the anode experiences structural changes in the graphite material, particularly related to phase transitions among different dilute lithium occupation stages.

For each of the 15 settled open circuit voltages, the experimental frequency responses were obtained through the GEIS measurements. The related Nyquist plots, showing the real and imaginary parts of the impedance Eq. (4), are reported in Fig. 5. It is worth noting that the actual values of the open circuit voltages are slightly different with respect to the settled ones because of the relaxion rest, as reported in Table 2.

After that, for each open circuit voltage, by fixing the ohmic resistance R_s (taken from the intersection with the real axis of the Nyquist plot) and the related diffusion capacitance, C_d, equal to the differential capacitance parameter, C_i, (obtained from the time-domain test) and

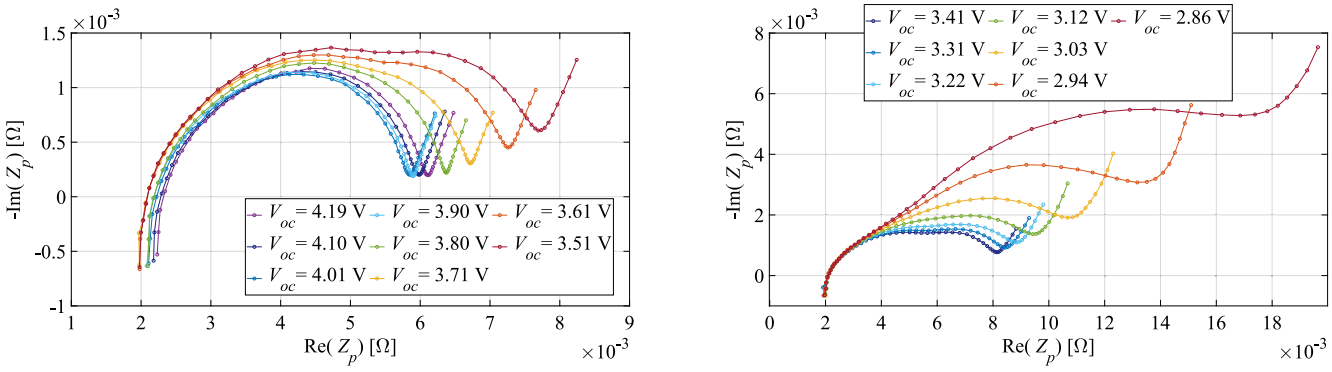

Fig. 5. Experimental GEIS measurement results.

Table 2
Electric circuit parameters and R^2.

V_{oc} [V]	R_s [mΩ]	R_{SEI} [mΩ]	C_{SEI} [F]	R_{ct} [mΩ]	C_{dl} [F]	R_d [mΩ]	C_d [F]	R^2_{Rp}	R^2_{Cp}
2.86	2.066	8.239	8.151	3.504	0.5477	55.80	846.7	0.9945	0.9991
2.94	2.106	5.927	5.481	2.824	0.4138	40.45	1081	0.9952	0.9996
3.03	2.067	4.458	4.718	2.648	0.3411	25.83	1432	0.9960	0.9986
3.12	2.080	3.624	4.727	2.566	0.3106	18.12	1803	0.9958	0.9975
3.22	2.073	3.204	5.318	2.583	0.3056	15.52	2520	0.9956	0.9983
3.31	2.066	2.982	5.789	2.604	0.2952	14.14	3532	0.9956	0.9983
3.41	2.075	2.850	5.644	2.548	0.2861	13.45	5064	0.9954	0.9982
3.51	2.072	2.705	4.792	2.363	0.2724	12.84	7409	0.9956	0.9976
3.61	2.063	2.578	3.771	2.152	0.2517	13.29	12,651	0.9956	0.9969
3.71	2.071	2.529	2.088	1.739	0.2205	47.88	76,600	0.9957	0.9944
3.80	2.180	2.581	1.002	1.271	0.1832	44.99	92,904	0.9946	0.9885
3.90	2.174	2.398	0.6963	1.007	0.1718	23.22	43,786	0.9935	0.9852
4.01	2.222	2.278	0.7440	1.059	0.1752	27.03	45,951	0.9956	0.9884
4.10	2.295	2.306	0.6876	1.087	0.1635	23.71	38,370	0.9957	0.9896
4.19	2.343	2.358	0.6428	1.113	0.1538	6.847	11,473	0.9954	0.9890

applying the fitting procedure to Eq. (4), minimizing Eq. (7), parameters R_{SEI}, C_{SEI}, R_{ct}, C_{dl}, and R_d were found. All the parameters are reported in Table 2.

Fig. 6 shows the experimental equivalent resistance and experimental equivalent capacitance as functions of the frequency, together with the related modeled data. Through those figures, it is possible to recognize the good agreement between the experimental and modeled data. Moreover, the coefficient of determination (R^2) was calculated and reported in Table 2. The latter confirms the goodness of the proposed UESS model in the frequency domain. In particular, the comparison between the experimental and modeled equivalent resistance and capacitance values shows very good agreement in the whole frequency range and, for all the settled voltages, R^2 is >0.99 for the equivalent resistance and 0.98 for the equivalent capacitance.

To validate the proposed UESS model in the time domain, parameter C_d was fitted as a piecewise constant function with 166 intervals, because it was very difficult to find a mathematical expression that was able to model the behavior reported in Fig. 4b. On the other hand, parameters R_s, R_{SEI}, C_{SEI}, R_{ct}, C_{dl}, and R_d were fitted using the following polynomial expressions, with the least square method, as functions of voltage V_{oc}:

$$
\begin{aligned}
R_s(V_{oc}) &= 3.266\cdot10^{-4}\cdot V_{oc}^2 - 2.132\cdot10^{-3}\cdot V_{oc} + 5.531\cdot10^{-3}\\
R_{SEI}(V_{oc}) &= 1.580\cdot10^{-2}\cdot V_{oc}^4 - 2.324\cdot10^{-1}\cdot V_{oc}^3 + 1.278\cdot V_{oc}^2 - 3.117\cdot V_{oc} + 2.847\\
C_{SEI}(V_{oc}) &= -88.84\cdot V_{oc}^5 + 1.607\cdot10^{3}\cdot V_{oc}^4 - 1.157\cdot10^{4} V_{oc}^3 + 4.142\cdot10^{4}\cdot V_{oc}^2 - 7.375\cdot10^{4}\cdot V_{oc} + 5.225\cdot10^{4}\\
R_{ct}(V_{oc}) &= 1.153\cdot10^{-2}\cdot V_{oc}^4 - 1.615\cdot10^{-1}\cdot V_{oc}^3 + 8.433\cdot10^{-1}\cdot V_{oc}^2 - 1.947\cdot V_{oc} + 1.681\\
C_{dl}(V_{oc}) &= 1.290\cdot V_{oc}^4 - 1.853\cdot10^{1}\cdot V_{oc}^3 + 9.946\cdot10^{1}\cdot V_{oc}^2 - 2.360\cdot10^{2}\cdot V_{oc} + 2.099\cdot10^{2}\\
R_d(V_{oc}) &= -4.073\cdot10^{-2}\cdot V_{oc}^4 + 3.606\cdot10^{-1}\cdot V_{oc}^3 - 7.334\cdot10^{-1}\cdot V_{oc}^2 - 1.080\cdot V_{oc} + 3.434.
\end{aligned}
\tag{8}
$$

Finally, Fig. 7 shows the parameters R_s, R_{SEI}, C_{SEI}, R_{ct}, C_{dl}, and R_d, as functions of voltage V_{oc}, along with their fitting functions, indicating a good agreement between them.

5. Model validation

To validate the proposed UESS model in the time domain, three different driving cycles with one electric vehicle (EV) were used. The three driving cycles were the New European Driving Cycle (NEDC), Supplemental Federal Test Procedure (SC03), and Worldwide Harmonized Light Vehicles Test Procedure (WLTP), as reported in Fig. 8. The EV chosen for these tests was the Volkswagen e-Up!, whose parameters, taken from [47], are reported in Table 3. The mechanical power required by the EV was calculated using the following mathematical equation:

$$P_m = \left(M_e a + \frac{1}{2} C_D S \rho v^2 + C_v M g \cos\alpha + M g \sin\alpha\right)\cdot v, \tag{9}$$

where v is the EV speed, a is the EV acceleration, g is the gravitational acceleration, α is the road slope, and M_e is the total inertial mass,

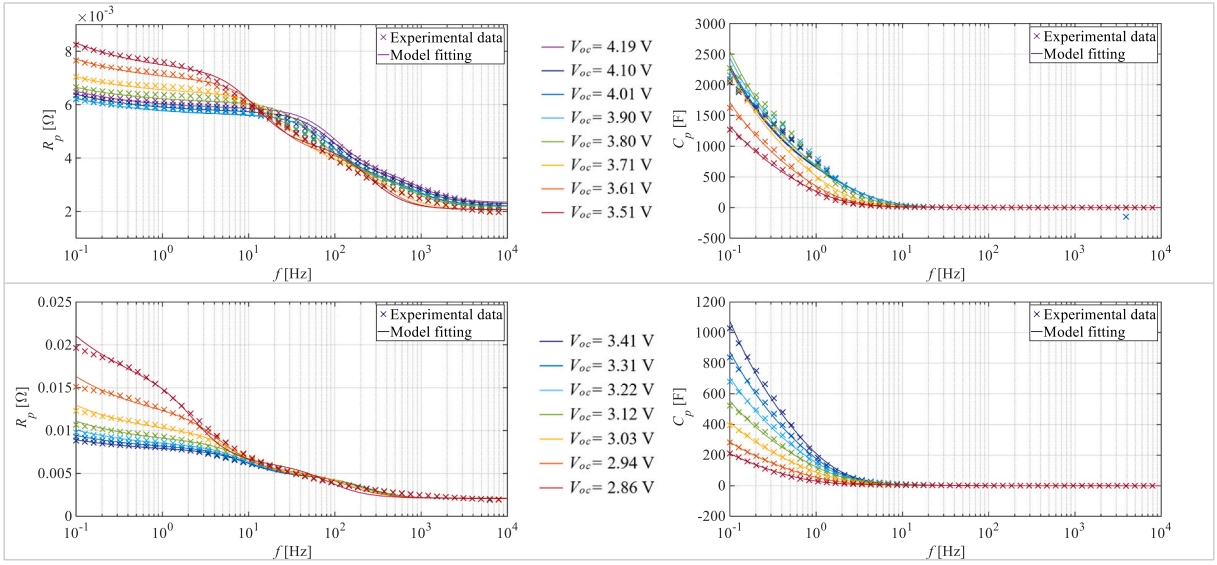

Fig. 6. Equivalent resistance and capacitance values as functions of the frequency.

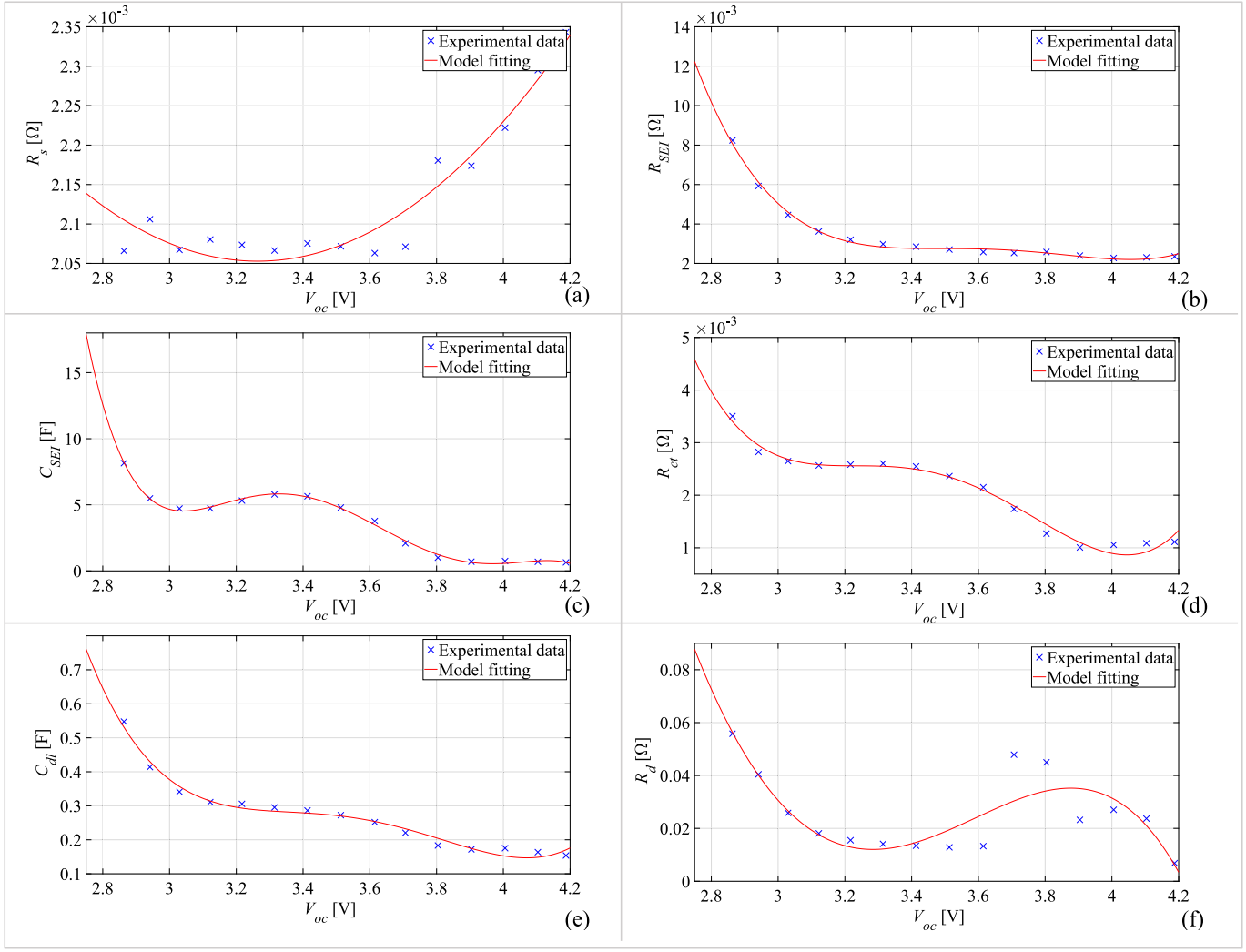

Fig. 7. Battery parameters and related fitting functions.

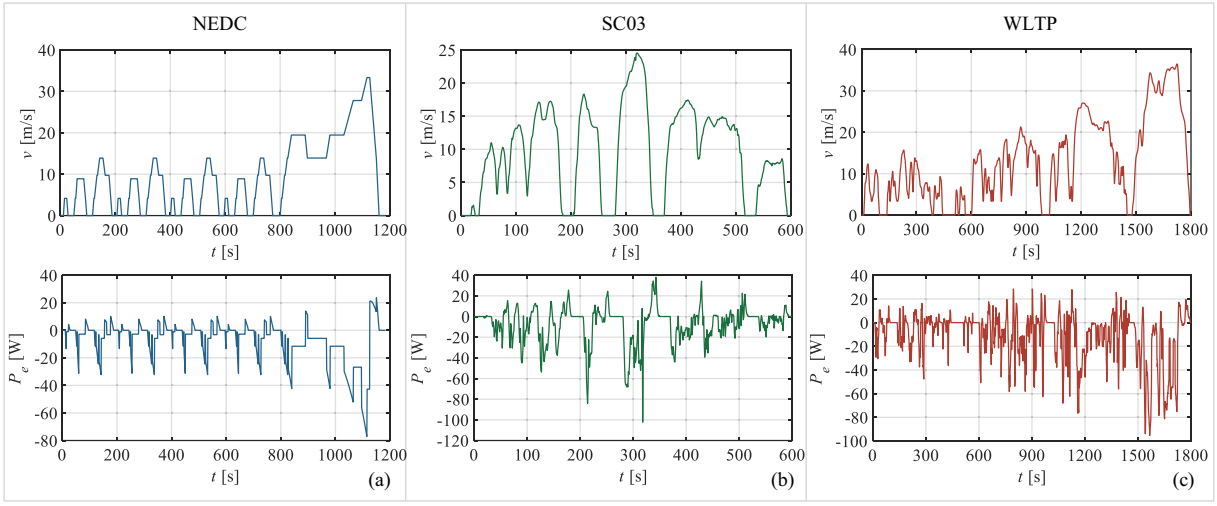

Fig. 8. Speed and electric power profiles for a) NEDC; b) SC03; c) WLTP.

Table 3
EV parameters.

EV	e-Up!
Curb weight M [kg]	1139
Aerodynamic coefficient C_D	0.308
Frontal surface S [m^2]	2.09
Rolling friction C_V	0.007
Air density ρ [kg/m^3]	1.184
Charging global efficiency η_{cha}	0.431
Discharging global efficiency η_{dis}	0.804
Battery Energy Capacity [kWh]	18.7

including all the rotating parts, which was obtained by increasing EV mass M by a factor of 10 %. All the other parameters are defined in Table 3. The mass of the EV was supposed to be augmented by adding four 70 kg people.

The electric power profiles exchanged with the battery pack of the EV, for each driving cycle, were obtained considering the global efficiencies related to traction and braking operations as follows:

$$\begin{cases} P_e = \eta_{cha} P_m, \quad P_m < 0 \\ P_e = \dfrac{P_m}{\eta_{dis}}, \quad P_m \geq 0. \end{cases} \tag{10}$$

Only one LiB cell was used in the validation of the experimental tests. Therefore, the electric power profiles, P_e, were scaled to fit the energy of a single LiB cell by dividing the requested power by the ratio between the total battery energy capacity and energy of the single LiB cell under test. These power profiles are reported in Fig. 8.

All three driving cycle tests were performed at the same room temperature (20 °C) used for the characterization procedure to avoid changes in the battery parameters with temperature. It is worth noting that, in the proposed procedure, the battery current was very low both in the open circuit voltage measurement and in GEIS measurements, but could reach 3C in the driving cycles, as can be seen from Fig. 9. Therefore, the battery temperature could increase even if the room temperature was fixed. Nevertheless, the overall shape of the driving cycles is composed of intervals in which the current is very low or nil, which made the temperature change negligible. In fact, Fig. 10 shows the temperature trends during the three driving cycles, and it is possible to note that the maximum increase in temperature was about 2 °C.

The three scaled electric power profiles were given as input for the real LiB cell, using the experimental setup reported in the previous section, and repeated until the battery voltage reached the minimum allowed threshold of 2.75 V. During the tests, both the experimental battery current and voltage were sampled and stored. Finally, to test the goodness of the proposed UESS model, the same experimental battery current profiles were used as inputs of the model.

Fig. 11 shows a comparison between the experimental and modeled battery voltages for the three cases, together with the absolute and relative percentage errors. As can be seen from the figures, the UESS model fits the behaviors of the battery in the different scenarios very well. In particular, in the range of 4.2–3.6 V, for all the driving cycles, the model almost perfectly fits the real behavior of the battery, with an absolute error of <40 mV and a relative error of <1 %. In the range of 3.6–2.75 V, for all the driving cycles, the absolute error was <70–80 mV, and the relative error was <2–2.5 %. On the other hand, only in proximity to the minimum cut-off voltage of 2.75 V, for the NEDC profile, the absolute error could reach 127 mV, and the relative error could reach 4.6 %. For the WLTP profile, the absolute error could reach 280 mV, and the relative error could reach 9.6 %. This could be because, at low SOC, the open circuit voltage curve (Fig. 4a) is very steep. Thus, small errors

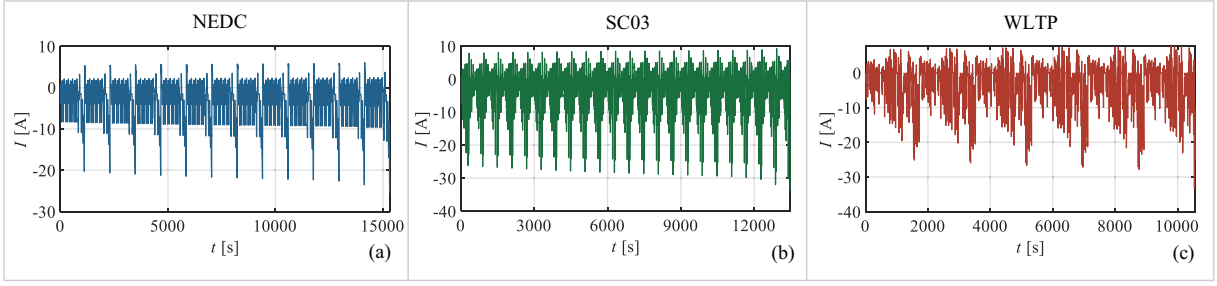

Fig. 9. Experimental battery current profiles: a) NEDC; b) SC03; c) WLTP.

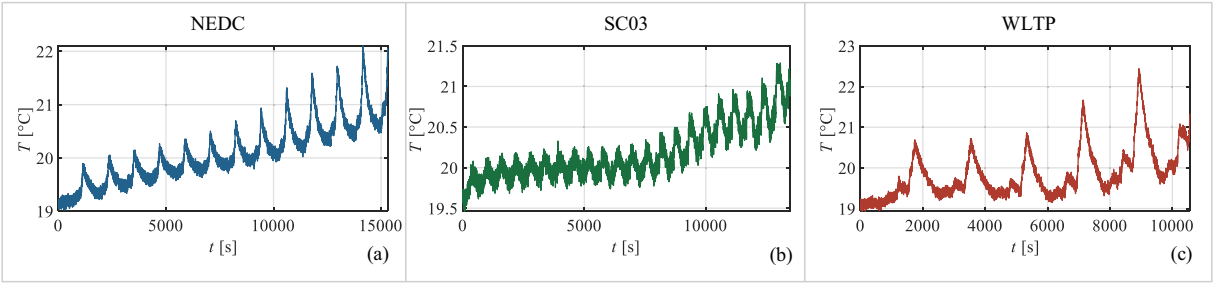

Fig. 10. Temperature profiles for a) NEDC; b) SC03; c) WLTP.

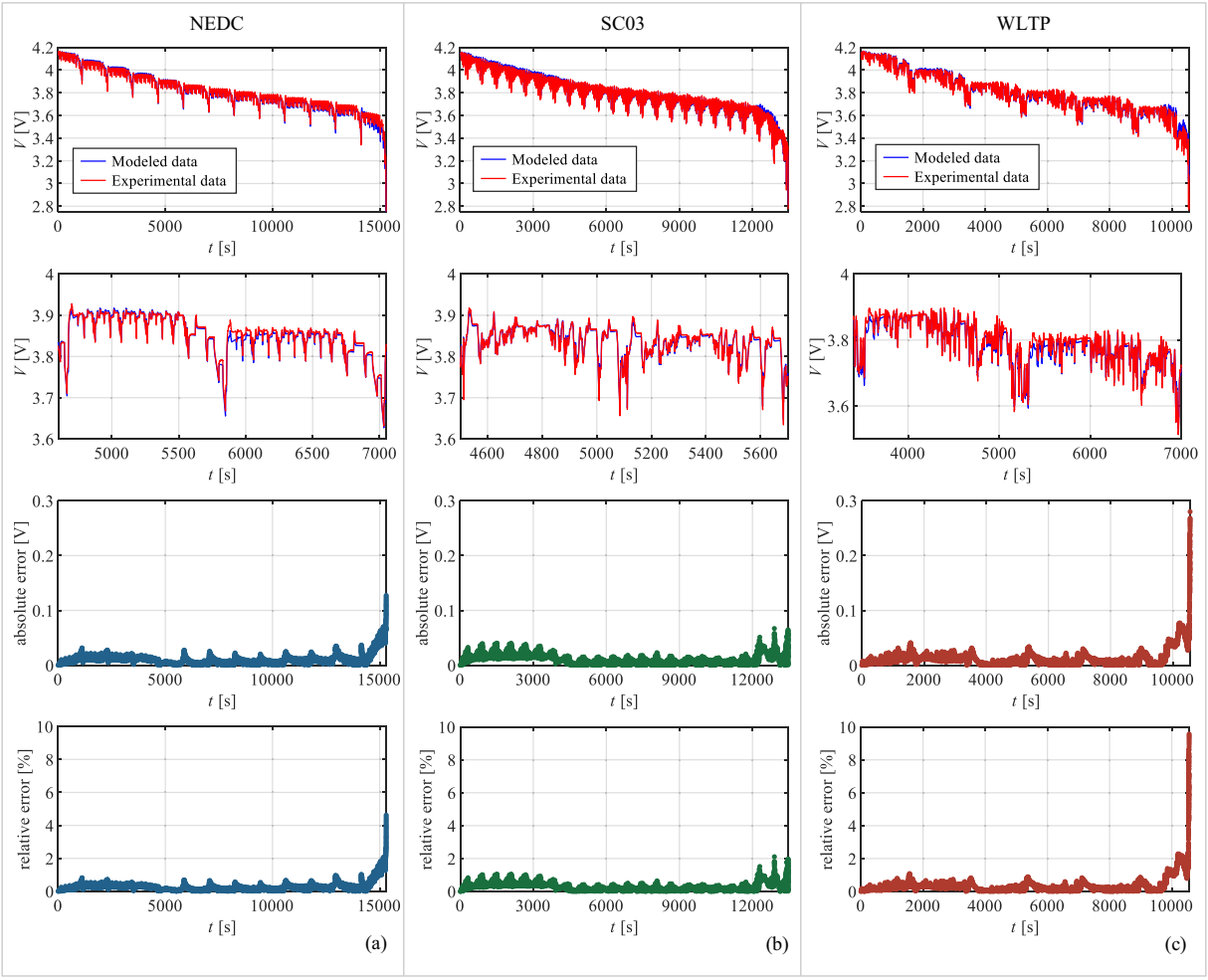

Fig. 11. Experimental and modeled battery voltages and relative voltage errors: a) NEDC; b) SC03; c) WLTP.

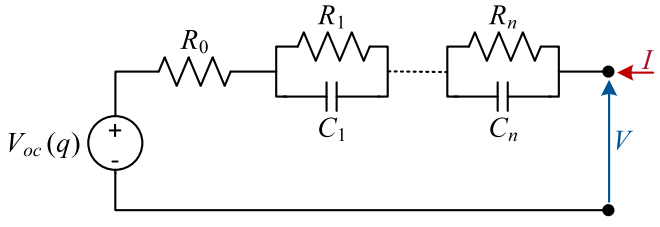

Fig. 12. *n*th-order Thevenin model.

in parameter estimation, which have a minimal impact at higher SOC, can lead to a worse battery voltage prediction. In addition, particularly at low SOC, the value of the battery current can increase the battery's internal resistance [48]. However, the inclusion of the current effect into the model is outside the scope of this work but would be worth deeper investigation in future works. Nevertheless, apart from the final part of the voltage curve, the model shows very good accuracy. For most applications, such as EVs, the range in which the battery is exploited is limited to 20–80 % of the SOC [49], which corresponds to the voltage range in which the UESS showed a very good fit.

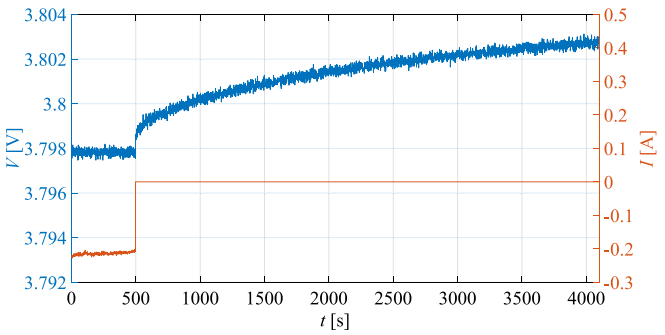

Fig. 13. Battery current and voltage during a relaxation transient.

6. Discussion

To assess the advantages and disadvantages of the UESS model applied to LiBs, a comparison was made with the most used Thevenin models of different orders. In particular, the zeroth-, first-, second-, and third-order Thevenin models, with two, four, six, and eight parameters respectively, were used to simulate the same three driving cycles. As reported in [15] and shown in Fig. 12, the *n*th-order Thevenin model consists of an ideal voltage source, which is a function of SOC, a series resistor R_0 that represents the ohmic resistance (like R_s in the UESS model), and many parallel R_kC_k branches as the order of the model.

To characterize these Thevenin models, the different parameters were estimated using a procedure similar to the one reported in [50]. For all the Thevenin models, the open circuit voltage curve of Fig. 4a was implemented in a look-up table and modeled by the ideal voltage source as a function of q. The other parameters were estimated through the time domain analysis of the battery voltage responses obtained during the relaxation intervals after the CV stages and before the beginning of the GEIS measurements, for the different open circuit voltages. In fact, for each of these intervals, during the CV stage, the battery current decayed up to 200 mA, allowing the parallel RC branches to reach a steady state. Then, the current was set to zero, leading to a current step ΔI of 200 mA, and the battery was left at rest for 1 h, thus a relaxation transient was observed for each open circuit voltage. Fig. 13 shows, as an example, this relaxation transient related to the open circuit voltage of 3.8 V.

During these relaxation intervals, the battery voltage can be expressed as follows:

$$V(t) = V_{oc}(q) + R_0\Delta I + \sum_{k=1}^{n} R_k\Delta I\left(1 - e^{-\frac{t}{R_kC_k}}\right). \tag{11}$$

Therefore, the ohmic resistance R_0 was estimated as the ratio between the instantaneous voltage drop and the current step. After that, this voltage drop was eliminated, and the remaining part of the voltage response was fitted to determine the other R_kC_k parameters using a number of exponential terms corresponding to the order of the model. For the sake of simplicity, all these values were put in look-up tables for simulations.

As indicators of the overall goodness of the different electric models, the R^2, mean absolute error (MAE), mean relative error (MRE), root mean square error (RMSE), and normalized root mean square error (NRMSE) were calculated for each driving cycle. The NRMSE was normalized based on the mean value of the experimental battery voltage. From Table 4, which reports the values of these indicators, it is possible to confirm the good agreement between the experimental and modeled data of the proposed UESS model, highlighting its superior accuracy compared to the Thevenin models across all three driving cycles. Although the UESS model may be slightly more complex than the zeroth-, first-, and second-order Thevenin models, its improved accuracy makes it a valuable choice for implementation. Furthermore, when comparing the UESS model to the third-order Thevenin model, which has one parameter more (eight), the latter exhibited significantly lower accuracy.

Finally, a further comparison was conducted with other results obtained in the literature. In [51], the authors showed that the second-order Thevenin model tested using the NEDC profile, resulted in an MAE of 18.4 mV, which is higher than the one obtained using the UESS model. In [52], the authors compared three battery models: the first- and second-order Thevenin model with the open circuit voltage curve modeled using the Nernst equation, and the second-order Thevenin model with the open circuit voltage curve modeled using a modified Nernst equation. From this comparison, they showed that the NRMSE obtained for the NEDC profile was 0.444 %, 0.424 %, and 0.421 %, respectively, which were higher than the one obtained with the UESS model. In [53], the authors conducted a comparison among several electric models for LiBs. In particular, they used the zeroth-, first-, and second-order Thevenin models. In all cases, the open circuit voltage curves were stored in look-up tables. Starting from these three electric models, they derived a total of eight different models based on factors that influence their parameters. In most cases, the open circuit voltage curve considered the voltage hysteresis, and the other parameters varied as a function of SOC, current, and current direction, making them much more complex than the UESS model. Nevertheless, from the comparison, they showed that for the WLTP profile, the MRE ranged from about 0.18 % to 0.46 %. This range encompasses the MRE obtained with the UESS model. Moreover, the authors calculated the MRE by considering the average of the MREs obtained for three different initial SOC levels (25 %, 50 %, and 75 %). For each of them, the initial open circuit voltage was adjusted to have no error at the beginning of each test. In this way, the average of the MREs was lower than the one obtained in the UESS model, where the WLTP test was repeated starting from a fully charged battery until reaching the minimum cut-off voltage. In [19], the authors proposed a fractional order model that is similar to the second-order Thevenin model but with two ZARC elements instead of the RC ones, resulting in a total of eight parameters. They tested the model using the Urban Dynamometer Driving Schedule (UDDS) profile and obtained an MAE of 15.4 mV, MRE of 0.49 %, and RMSE of 20.9 mV. Although the UDDS profile was not tested in the present work, these errors were higher than the ones obtained with the UESS model for all three driving cycles tested.

Table 4
Indicators of the goodness of fit.

Driving cycle	Model	R^2	MAE [mV]	MRE	RMSE [mV]	NRMSE
NEDC	Zeroth-order Thevenin	0.905	23.7	0.640	49.4	1.29
	First-order Thevenin	0.968	19.5	0.521	28.7	0.752
	Second-order Thevenin	0.977	16.1	0.432	24.5	0.640
	Third-order Thevenin	0.978	15.7	0.424	24.1	0.630
	UESS	0.992	10.7	0.286	14.2	0.372
SC03	Zeroth-order Thevenin	0.898	32.2	0.866	53.0	1.40
	First-order Thevenin	0.961	22.5	0.605	32.9	0.867
	Second-order Thevenin	0.975	17.5	0.473	26.0	0.686
	Third-order Thevenin	0.978	16.4	0.444	24.8	0.653
	UESS	0.994	10.1	0.266	12.9	0.340
WLTP	Zeroth-order Thevenin	0.925	32.6	0.877	48.8	1.28
	First-order Thevenin	0.955	24.8	0.670	38.0	1.00
	Second-order Thevenin	0.976	18.7	0.504	27.8	0.731
	Third-order Thevenin	0.979	17.0	0.460	26.1	0.685
	UESS	0.989	12.4	0.337	18.9	0.498

7. Conclusion

In the present work, the equivalent circuit model used in [40–42] to model EDLCs and LiCs was proven to be suitable for predicting the battery behavior in both the frequency- and time-domain under fixed temperature. In fact, in LiBs, as in EDLCs and LiCs, the energy is stored or released only through the electric port. Therefore, it could be considered to be a large equivalent capacitor. Unlike EDLCs, in which the electric energy is stored as dielectric energy through the electric field in the dielectric medium, in LiBs, the electric energy is stored as chemical energy through chemical reactions (intercalations and de-intercalations of lithium-ions). In an LiC, which is a hybridization between an EDLC and LiB, the electric energy in stored in both ways.

The proposed model with seven parameters is composed of a series of four impedance terms: an ohmic resistor, a parallel RC branch related to the SEI, another one related to the charge transfer and double layer effect, and a finite space Warburg element. The latter can model both the lithium\lithium-ion diffusion into the electrodes\electrolyte and the main capacitance related to the energy stored in the battery.

The model parameters were estimated using a combined procedure based on both time- and frequency-domain methods. The battery discharge performed at a low-current rate was used to extract the differential capacitance of the battery, which corresponds to the diffusion capacitance of the Warburg element. The other parameters were extracted through the GEIS measurements in a frequency range of 10 kHz–100 mHz for different open circuit voltages. To use the proposed model in the time domain, the values of the diffusion capacitance were stored in a look-up table, while the other parameters were fitted as a function of the open circuit voltage using polynomial expressions.

Finally, the validation of the proposed model in the time domain was carried out through three standard driving cycles (NEDC, SC03, and WLTP) with one EV. The related electric power profiles were obtained using Eqs. (9) and (10), and scaled for the battery cell under test. The experimental results of the battery voltage were compared with those obtained through the simulations and showed a very good match. Therefore, the validation of the proposed model, along with the parameter estimation procedure, can be highly beneficial for unifying the modeling of different electrochemical storage systems, such as LiBs, EDLCs, and LiCs, leading to the UESS model.

Furthermore, the UESS model compared to other models present in the literature demonstrated a better accuracy as quantified through different indicators of the goodness of fit. In particular, in the usual working range of the battery, the relative error was lower than 1 %. In the last part of the voltage curve, the error increased to about 4.6 % and 9.6 % for the NEDC and WLTP profiles, respectively. This could be because, at low SOC, small errors in parameter estimation can have a high impact on the battery voltage prediction due to the steepness of the open circuit voltage curve in that region. Moreover, the effect of the current rate was not considered in the UESS model and may affect the battery's internal resistance, thus the output battery voltage. The latter effect was outside of the scope of the present article but could be further analyzed in future works. In addition, also the effect of the temperature on the parameters can be taken into account to further extend the model working in a wide temperature range.

CRediT authorship contribution statement

Simone Barcellona: Conceptualization, Methodology, Formal analysis, Investigation, Writing – original draft, Visualization, Data curation, Writing – review & editing. **Silvia Colnago:** Conceptualization, Methodology, Formal analysis, Investigation, Writing – original draft, Visualization, Data curation, Writing – review & editing. **Lorenzo Codecasa:** Formal analysis, Writing – review & editing, Supervision. **Luigi Piegari:** Resources, Writing – review & editing, Supervision.

Declaration of competing interest

The authors declare that they have no known competing financial interests or personal relationships that could have appeared to influence the work reported in this paper.

Data availability

The authors are unable or have chosen not to specify which data has been used.

References

[1] R. Zito, H. Ardebili, Energy Storage, Wiley, 2019, https://doi.org/10.1002/9781119083979.
[2] Q. Abbas, M. Mirzaeian, M.R.C. Hunt, P. Hall, R. Raza, Current state and future prospects for electrochemical energy storage and conversion systems, Energies 13 (2020) 5847, https://doi.org/10.3390/en13215847.
[3] M. Winter, R.J. Brodd, What are batteries, fuel cells, and supercapacitors? Chem. Rev. 104 (2004) 4245–4270, https://doi.org/10.1021/cr020730k.
[4] S. Barcellona, L. Piegari, Lithium ion battery models and parameter identification techniques, Energies 10 (2017) 2007, https://doi.org/10.3390/en10122007.
[5] Y. Zheng, Z. Shi, D. Guo, H. Dai, X. Han, A simplification of the time-domain equivalent circuit model for lithium-ion batteries based on low-frequency electrochemical impedance spectra, J. Power Sources 489 (2021), 229505, https://doi.org/10.1016/j.jpowsour.2021.229505.
[6] S. Barcellona, S. Colnago, P. Montrasio, L. Piegari, Integrated electro-thermal model for Li-ion battery packs, Electronics 11 (2022) 1537, https://doi.org/10.3390/electronics11101537.
[7] C. Forgez, D. Vinh Do, G. Friedrich, M. Morcrette, C. Delacourt, Thermal modeling of a cylindrical LiFePO4/graphite lithium-ion battery, J. Power Sources 195 (2010) 2961–2968, https://doi.org/10.1016/j.jpowsour.2009.10.105.
[8] S. Barcellona, L. Piegari, Integrated electro-thermal model for pouch lithium ion batteries, Math. Comput. Simul. 183 (2021) 5–19, https://doi.org/10.1016/j.matcom.2020.03.010.
[9] S. Barcellona, S. Colnago, G. Dotelli, S. Latorrata, L. Piegari, Aging effect on the variation of Li-ion battery resistance as function of temperature and state of charge, J. Energy Storage 50 (2022), 104658, https://doi.org/10.1016/j.est.2022.104658.
[10] M.-K. Tran, M. Mathew, S. Janhunen, S. Panchal, K. Raahemifar, R. Fraser, M. Fowler, A comprehensive equivalent circuit model for lithium-ion batteries, incorporating the effects of state of health, state of charge, and temperature on model parameters, J. Energy Storage 43 (2021), 103252, https://doi.org/10.1016/j.est.2021.103252.
[11] H. He, R. Xiong, J. Fan, Evaluation of Lithium-ion battery equivalent circuit models for state of charge estimation by an experimental approach, Energies 4 (2011) 582–598, https://doi.org/10.3390/en4040582.
[12] Yoon-Ho Kim, Hoi-Doo Ha, Design of interface circuits with electrical battery models, IEEE Trans. Ind. Electron. 44 (1997) 81–86, https://doi.org/10.1109/41.557502.
[13] F. Feng, R. Lu, G. Wei, C. Zhu, Online estimation of model parameters and state of charge of LiFePO4 batteries using a novel open-circuit voltage at various ambient temperatures, Energies 8 (2015) 2950–2976, https://doi.org/10.3390/en8042950.
[14] C. Zhang, W. Allafi, Q. Dinh, P. Ascencio, J. Marco, Online estimation of battery equivalent circuit model parameters and state of charge using decoupled least squares technique, Energy 142 (2018) 678–688, https://doi.org/10.1016/j.energy.2017.10.043.
[15] A. Hentunen, T. Lehmuspelto, J. Suomela, Time-domain parameter extraction method for Thévenin-equivalent circuit battery models, IEEE Trans. Energy Convers. 29 (2014) 558–566, https://doi.org/10.1109/TEC.2014.2318205.
[16] X. Wang, X. Wei, H. Dai, Estimation of state of health of lithium-ion batteries based on charge transfer resistance considering different temperature and state of charge, J. Energy Storage 21 (2019) 618–631, https://doi.org/10.1016/j.est.2018.11.020.
[17] D. Andre, M. Meiler, K. Steiner, H. Walz, T. Soczka-Guth, D.U.U. Sauer, C. Wimmer, T. Soczka-Guth, D.U.U. Sauer, Characterization of high-power lithium-ion batteries by electrochemical impedance spectroscopy. I. Experimental investigation, J. Power Sources 196 (2011) 5334–5341, https://doi.org/10.1016/j.jpowsour.2010.12.102.
[18] Y. Wang, M. Li, Z. Chen, Experimental study of fractional-order models for lithium-ion battery and ultra-capacitor: modeling, system identification, and validation, Appl. Energy 278 (2020), 115736, https://doi.org/10.1016/j.apenergy.2020.115736.
[19] Y. Wang, G. Gao, X. Li, Z. Chen, A fractional-order model-based state estimation approach for lithium-ion battery and ultra-capacitor hybrid power source system considering load trajectory, J. Power Sources 449 (2020), 227543, https://doi.org/10.1016/j.jpowsour.2019.227543.
[20] U. Westerhoff, T. Kroker, K. Kurbach, M. Kurrat, Electrochemical impedance spectroscopy based estimation of the state of charge of lithium-ion batteries, J. Energy Storage 8 (2016) 244–256, https://doi.org/10.1016/j.est.2016.09.001.
[21] Y. Wang, J. Tian, Z. Sun, L. Wang, R. Xu, M. Li, Z. Chen, A comprehensive review of battery modeling and state estimation approaches for advanced battery management systems, Renew. Sustain. Energy Rev. 131 (2020), 110015, https://doi.org/10.1016/j.rser.2020.110015.

[22] H. Dai, T. Xu, L. Zhu, X. Wei, Z. Sun, Adaptive model parameter identification for large capacity Li-ion batteries on separated time scales, Appl. Energy 184 (2016) 119–131, https://doi.org/10.1016/j.apenergy.2016.10.020.
[23] T. Momma, M. Matsunaga, D. Mukoyama, T. Osaka, Ac impedance analysis of lithium ion battery under temperature control, J. Power Sources 216 (2012) 304–307, https://doi.org/10.1016/j.jpowsour.2012.05.095.
[24] B.V. Ratnakumar, M.C. Smart, L.D. Whitcanack, R.C. Ewell, The impedance characteristics of Mars exploration rover Li-ion batteries, J. Power Sources 159 (2006) 1428–1439, https://doi.org/10.1016/j.jpowsour.2005.11.085.
[25] D. Anseán, V.M. García, M. González, J.C. Viera, C. Blanco, J.L. Antuña, DC internal resistance during charge: analysis and study on LiFePO<inf>4</inf> batteries, in: 2013 World Electr. Veh. Symp. Exhib, 2013, pp. 1–11, https://doi.org/10.1109/EVS.2013.6914746.
[26] J. Gomez, R. Nelson, E.E. Kalu, M.H. Weatherspoon, J.P. Zheng, Equivalent circuit model parameters of a high-power Li-ion battery: thermal and state of charge effects, J. Power Sources 196 (2011) 4826–4831, https://doi.org/10.1016/j.jpowsour.2010.12.107.
[27] A. Fotouhi, K. Propp, D.J. Auger, Electric vehicle battery model identification and state of charge estimation in real world driving cycles, in: 2015 7th Comput, Sci. Electron. Eng. Conf, IEEE, 2015, pp. 243–248, https://doi.org/10.1109/CEEC.2015.7332732.
[28] S. Barcellona, S. Grillo, L. Piegari, A simple battery model for EV range prediction: Theory and experimental validation, in: 2016 Int. Conf. Electr. Syst. Aircraft, Railw. Sh. Propuls. Road Veh. Int. Transp. Electrif. Conf., IEEE, 2016, pp. 1–7, https://doi.org/10.1109/ESARS-ITEC.2016.7841441.
[29] M. Brenna, F. Foiadelli, M. Longo, S. Barcellona, L. Piegari, Lithium-ion battery: a simplified modeling procedure and system simulation, in: 2016 Int. Symp. Power Electron. Electr. Drives, Autom. Motion, IEEE, 2016, pp. 1034–1040, https://doi.org/10.1109/SPEEDAM.2016.7525915.
[30] M. Hu, Y. Li, S. Li, C. Fu, D. Qin, Z. Li, Lithium-ion battery modeling and parameter identification based on fractional theory, Energy. 165 (2018) 153–163, https://doi.org/10.1016/j.energy.2018.09.101.
[31] G. Brando, A. Dannier, I. Spina, L. Piegari, Comparison of accuracy of different LiFePO<inf>4</inf> battery circuital models, in: 2014 Int. Symp. Power Electron. Electr. Drives, Autom. Motion, IEEE, 2014, pp. 1092–1097, https://doi.org/10.1109/SPEEDAM.2014.6872021.
[32] C.R. Birkl, D.A. Howey, Model identification and parameter estimation for LiFePO4 batteries, in: Hybrid Electr. Veh. Conf. 2013 (HEVC 2013), Institution of Engineering and Technology, 2013, https://doi.org/10.1049/cp.2013.1889 (pp. 2.1–2.1).
[33] S.S. Zhang, K. Xu, T.R. Jow, Electrochemical impedance study on the low temperature of Li-ion batteries, Electrochim. Acta 49 (2004) 1057–1061, https://doi.org/10.1016/j.electacta.2003.10.016.
[34] A. Barai, G.H. Chouchelamane, Y. Guo, A. McGordon, P. Jennings, A study on the impact of lithium-ion cell relaxation on electrochemical impedance spectroscopy, J. Power Sources 280 (2015) 74–80, https://doi.org/10.1016/j.jpowsour.2015.01.097.
[35] J. Schmitt, A. Maheshwari, M. Heck, S. Lux, M. Vetter, Impedance change and capacity fade of lithium nickel manganese cobalt oxide-based batteries during calendar aging, J. Power Sources 353 (2017) 183–194, https://doi.org/10.1016/j.jpowsour.2017.03.090.
[36] M. Oldenburger, B. Bedürftig, A. Gruhle, F. Grimsmann, E. Richter, R. Findeisen, A. Hintennach, Investigation of the low frequency Warburg impedance of Li-ion cells by frequency domain measurements, J. Energy Storage 21 (2019) 272–280, https://doi.org/10.1016/j.est.2018.11.029.
[37] F. Feng, R. Yang, J. Meng, Y. Xie, Z. Zhang, Y. Chai, L. Mou, Electrochemical impedance characteristics at various conditions for commercial solid–liquid electrolyte lithium-ion batteries: part. 2. Modeling and prediction, Energy 243 (2022), 123091, https://doi.org/10.1016/j.energy.2021.123091.
[38] Q.-K. Wang, Y.-J. He, J.-N. Shen, X.-S. Hu, Z.-F. Ma, State of charge-dependent polynomial equivalent circuit modeling for electrochemical impedance spectroscopy of Lithium-ion batteries, IEEE Trans. Power Electron. 33 (2018) 8449–8460, https://doi.org/10.1109/TPEL.2017.2780184.
[39] S.E. Li, B. Wang, H. Peng, X. Hu, An electrochemistry-based impedance model for lithium-ion batteries, J. Power Sources 258 (2014) 9–18, https://doi.org/10.1016/j.jpowsour.2014.02.045.
[40] V. Musolino, L. Piegari, E. Tironi, New full-frequency-range supercapacitor model with easy identification procedure, IEEE Trans. Ind. Electron. 60 (2013) 112–120, https://doi.org/10.1109/TIE.2012.2187412.
[41] S. Barcellona, F. Ciccarelli, D. Iannuzzi, L. Piegari, Modeling and parameter identification of lithium-ion capacitor modules, IEEE Trans. Sustain. Energy 5 (2014) 785–794, https://doi.org/10.1109/TSTE.2014.2301950.
[42] S. Barcellona, L. Piegari, A lithium-ion capacitor model working on a wide temperature range, J. Power Sources 342 (2017) 241–251, https://doi.org/10.1016/j.jpowsour.2016.12.055.
[43] S. Cruz-Manzo, P. Greenwood, An impedance model based on a transmission line circuit and a frequency dispersion Warburg component for the study of EIS in Li-ion batteries, J. Electroanal. Chem. 871 (2020), 114305, https://doi.org/10.1016/j.jelechem.2020.114305.
[44] T.J.I. Bromwich, An Introduction to the Theory of Infinite Series, American Mathematical Society, 2005.
[45] D. Guo, G. Yang, G. Zhao, M. Yi, X. Feng, X. Han, L. Lu, M. Ouyang, Determination of the differential capacity of lithium-ion batteries by the deconvolution of electrochemical impedance spectra, Energies 13 (2020) 915, https://doi.org/10.3390/en13040915.
[46] S. Li, S. Tsutsumi, S. Shironita, M. Umeda, Peak attribution of the differential capacity profile of a LiCoO2-based three-electrode Li-ion laminate cell, Electrochemistry 90 (2022) 21–00128, https://doi.org/10.5796/electrochemistry.21-00128.
[47] E.A. Grunditz, T. Thiringer, Performance analysis of current BEVs based on a comprehensive review of specifications, IEEE Trans. Transp. Electrif. 2 (2016) 270–289, https://doi.org/10.1109/TTE.2016.2571783.
[48] L. Chen, M. Zhang, Y. Ding, S. Wu, Y. Li, G. Liang, H. Li, H. Pan, Estimation the internal resistance of lithium-ion-battery using a multi-factor dynamic internal resistance model with an error compensation strategy, Energy Rep. 7 (2021) 3050–3059, https://doi.org/10.1016/j.egyr.2021.05.027.
[49] E.D. Kostopoulos, G.C. Spyropoulos, J.K. Kaldellis, Real-world study for the optimal charging of electric vehicles, Energy Rep. 6 (2020) 418–426, https://doi.org/10.1016/j.egyr.2019.12.008.
[50] L. Gurjer, P. Chaudhary, H.K. Verma, Detailed modelling procedure for lithium-ion battery using thevenin equivalent, in: 2019 IEEE Int. Conf. Electr. Comput. Commun. Technol., IEEE, 2019, pp. 1–6, https://doi.org/10.1109/ICECCT.2019.8869224.
[51] J. Meng, G. Luo, M. Ricco, M. Swierczynski, D.-I. Stroe, R. Teodorescu, Overview of lithium-ion battery modeling methods for state-of-charge estimation in electrical vehicles, Appl. Sci. 8 (2018) 659, https://doi.org/10.3390/app8050659.
[52] Y. Ghoulam, T. Mesbahi, P. Wilson, S. Durand, A. Lewis, C. Lallement, C. Vagg, Lithium-ion battery parameter identification for hybrid and electric vehicles using drive cycle data, Energies 15 (2022) 4005, https://doi.org/10.3390/en15114005.
[53] M. Auch, T. Kuthada, S. Giese, A. Wagner, Influence of Lithium-ion-battery equivalent circuit model parameter dependencies and architectures on the predicted heat generation in real-life drive cycles, Batteries 9 (2023) 274, https://doi.org/10.3390/batteries9050274.